

Supplemental Material

S1. Hybrid vs intermediate Bloch/Néel walls

In Lorentz TEM contrast is generated through the interaction of the electron beam and the magnetic induction component perpendicular to its path. This means that magnetic objects which have the same induction component projected through the thickness are indistinguishable in Lorentz TEM (without performing tomography). Hence it should be noted that what we refer to in this paper as a hybrid Bloch/Néel domain wall – that is with varying M_x and M_y throughout the thickness – is indistinguishable from an intermediate Bloch/Néel wall – one with constant magnetisation through the thickness with components perpendicular and parallel to the length of the wall (x and y components as detailed below). These two magnetic configurations are sketched in Fig. S1 which shows domains magnetized in the $\pm z$ direction and a wall which runs along the y direction. Fig. S1(a) has a hybrid domain wall with Néel type walls on the top and bottom surfaces and a Bloch type core in the middle. Fig. S1(b) shows an intermediate domain wall which is in a fixed direction through the thickness and orientated somewhere between a conventional Bloch or Néel type wall, i.e. the wall has both x and y components of magnetisation.

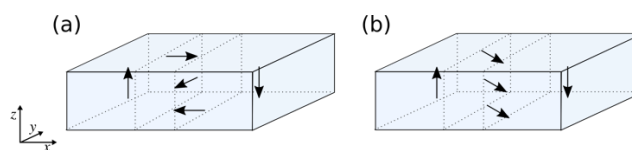


Figure S1. Illustrations of an out of plane magnetised material with (a) a hybrid domain wall and (b) an intermediate domain wall.

S2. AFM confirming contorted membrane surface

As discussed in the main text with regard to Fig 3., the Fresnel images taken at zero microscope rod tilt show magnetic contrast only expected from the sample when tilted, this lead us to conclude that the membrane surface is contorted. The contrast expected from skyrmionic multilayer samples with out-of-plane magnetisation varies in a predicable manner with tilt, hence varying the tilt while analyzing the contrast allows us to identify the true zero tilt, defined as when the imaging area is locally normal to the electron beam. This true zero tilt was often identified at around 10° from the microscope rod tilt, indicating severe buckling of the membrane. As the results of this paper depend critically on the tilt of the sample with respect to the electron beam we have performed atomic force microscope (AFM) to verify that the membrane surface is severely contorted. An image acquired from the $15\times$ sample, which is representative of the sample as a whole, is shown in Fig. S2(a). The right-hand side of this image shows the opaque silicon frame which is, as expected, flat. The left-hand side of this image shows the topography of the membrane and confirms it is severely buckled. A histogram of the surface tilt of the frame and membrane was constructed by analyzing the gradient of the AFM image. This histogram is shown in Fig. S2(b) and confirms that the membrane tilts are between approximately $\pm 15^\circ$ relative to the flat silicon frame.

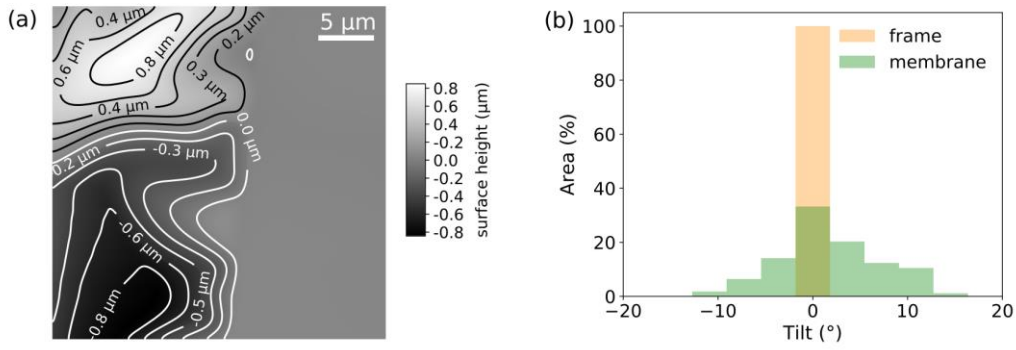


Figure S2. AFM image (a), which shows the membrane on the left and the thick Si frame on the right, confirm the sample surface to be severely buckled. The histogram (b) shows the variation in surface tilt of the membrane compared to the thick Si frame in the field of view of image (a).

S3&4. Fresnel images of 10× and 5× samples

Fresnel images of the 10× sample show the magnetic contrast variation with tilt as the 15× sample discussed in the main body of the paper (those show in Fig. 4), indicative of the film supporting hybrid domain walls. These images are shown in Fig. S3(a-c). The Fresnel image contrast is weaker from this sample compared to the 15× due to the reduced total magnetic thickness. As with the 15× sample, the 10× sample is severely buckled thus only some regions of Fig. S3(b) are at effective zero tilt with respect to the electron beam - one such region is indicated by the red circle on the left of the image. Images S3(a) and S3(c) are taken at relative tilts of -10° and $+10^\circ$ compared to image S3(b). The line traces shown in Fig S3(d) and S3(f) show characteristic domain contrast which reverses with tilt. The line trace in Fig S3(e) is of lower contrast and symmetric – indicating that this sample has walls with partial Bloch character. The dashed lines on the line traces show the position of the centre of each domain wall as a guide to the eye.

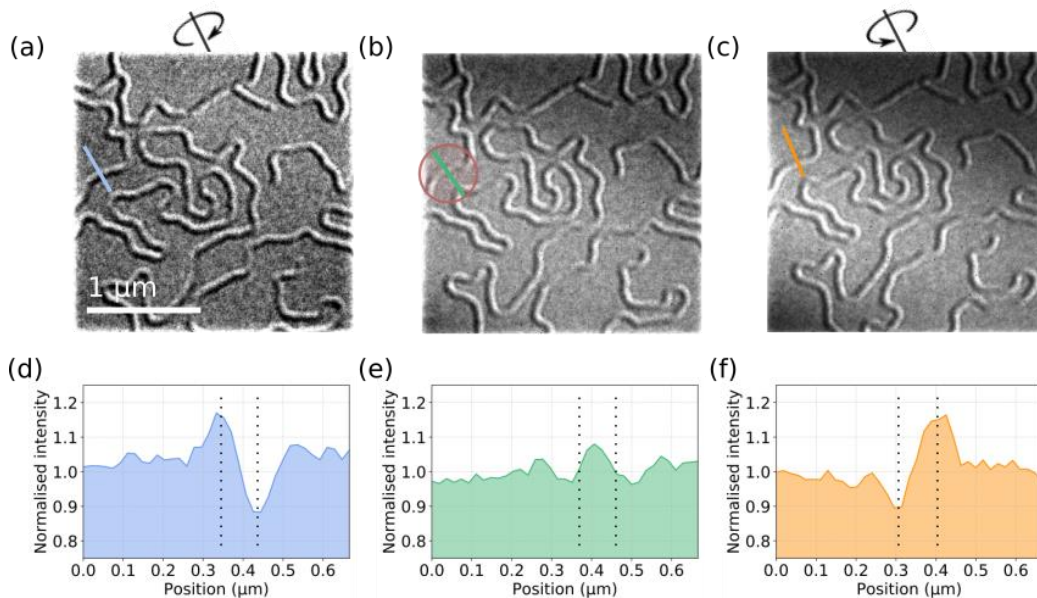


Figure S3. Fresnel images of 10× layer sample with closely spaced pairs of domain walls with varying local tilt at the blue lines to be (a) $+10^\circ$, (b) 0° and (c) -10° . The corresponding intensity line traces from these images, averaged over 10 lines, are shown in (d-f).

In the case of the $5\times$ sample the Fresnel image contrast does not provide clear evidence of the existence of hybrid domain walls. The images are shown in Fig S4(a-c) and have weaker contrast than the $10\times$ sample as expected. Image S4(b) is at approximate zero tilt, with image S4(a) at relative -9° and S4(c) at relative $+8^\circ$. Line traces taken across the same wall region of each Fresnel image are shown in Fig S4(d-f). This area was chosen to analyze because this area in images S4(a) and S4(c) shows unambiguous contrast reversal with tilt. The line trace in S4(d) and S4(f) shows contrast consistent with that arising from the domains which is above the background intensity variation that has reversed with tilt. The line trace in S4(e), through the same area at zero tilt, has no clearly discernible contrast above the background intensity variation.

The contrast in images S4(a) and S4(c) arises from an electron beam deflection proportional to $\sim 0.14B_{st}$ (from out of plane domains tilted at $8^\circ/9^\circ$). If this sample possessed hybrid walls even with only one layer having the Bloch structure, at zero tilt this would lead to a deflection proportional to $0.2B_{st}$. Hence, this proportion of Bloch type would lead to contrast in S4(b) at least as strong as images S4(a) and S4(c). As detailed later in this document, simulations show that for the $5\times$ sample the Bloch component may be very weak and therefore consistent with these observations of no discernable or a very weak Bloch component.

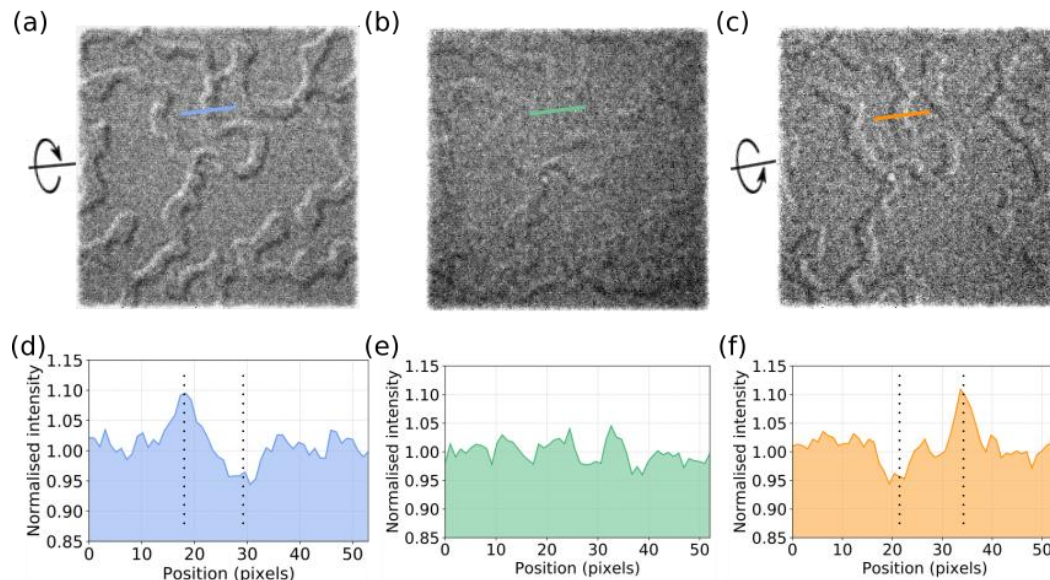


Figure S4. Fresnel images of $5\times$ layer sample with closely spaced pairs of domain walls with varying local tilt at the blue lines to be (a) $+9^\circ$, (b) 0° and (c) -8° . The corresponding intensity line traces from these images, averaged over 10 lines, are shown in (d-f). (Note that these images were not calibrated so lengths are in pixels, however the key point here is just to demonstrate the nature of the contrast not measure any quantitative spatial extent)

S5. Challenges of DPC of multilayer materials with out-of-plane magnetisation.

The technique of DPC relies on measuring the shifts of the central diffraction disk due to changes in integrated magnetic induction as it is scanned over a magnetic sample. The standard method of detecting these beam shifts is by using a quadrant detector, here the signal is summed in each quadrant and differences between signals measured in each quadrant are used to measure the beam shifts. This becomes challenging for materials with small integrated magnetic induction (small beam shifts) or materials which scatter strongly (uneven central diffraction disks). The relatively large thickness, of predominantly heavy metals, results in of skyrmionic multilayer samples strongly scattering the electron beam. For example, at normal incidence, the $15\times$ sample has a total thickness of 74.4 nm of which only 24.0 nm is magnetic.

Furthermore, these samples are magnetised out of plane and must be tilted to gain a component of integrated induction correctly orientated to produce a beam deflection proportional to $\sin(\theta)$, where θ is the sample tilt. Tilting of course further increases the projected thickness. This makes skyrmionic multilayer samples challenging for DPC.

For illustration, Fig. S5(a) shows an “ideal” disk – obtained from a permalloy film of thickness 8 nm – which can be compared to a disk from the 15 \times sample, S5(b), which is extremely uneven and has significantly lower counts than S5(a). These two images of disks are with the same aperture but taken at different camera lengths and with acquisition times of S5(a) 1 ms and S5(b) 3 ms.

From the $\times 15$ sample tilted by 10° the beam shifts are expected to be only a few μrad , this is tiny compared to the beam diameter of around 2.5 mrad seen in Fig. S5(b). It is also important to note, the image Fig. S5(b) is an example from one position in the scan, each diffraction disk from each scan position will be uneven in a different way due to different polycrystalline grains and grain boundaries satisfying different diffraction conditions. Remembering that the segmented detector aims to detect shifts by simply summing the signal in each quadrant for each scan position, the strong contrast variations seen in Fig. S5(b) result in changes to the quadrant signals much larger than the magnetic shift. Consequently, an image like Fig. S5(c) will be acquired which is clearly dominated by the crystallites, lacking the desired magnetic contrast. For a sample that scatters less strongly and has larger expected beam deflections, such as the disk from 8 nm Permalloy in Fig 5(a), the segmented detector will successfully detect the beam shifts and a map of the magnetic induction can be produced. By using a pixelated detector, we are able to suppress the diffraction contrast by measuring the beam deflections more directly by tracking shifts in the edge of the disk (ref [35] in the main text). By comparison to S5(c), image S5(d) shows the clear magnetic contrast we are able to regain by using the pixelated detector.

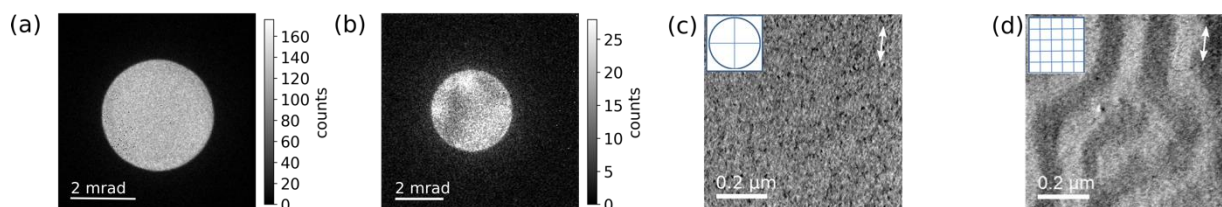


Figure S5. (a) Image of diffraction disk in detector plane from 8 nm of Permalloy for comparison with (b) an example diffraction disk taken from the $\times 15$ sample. For skyrmionic multilayers, the strong diffraction contrast [visible in (b)] and the relatively small deflection [expected to be only a few μrad] result in no observable magnetic contrast with (c) a segmented detector and (d) clearly visible contrast when using a pixelated detector. The double headed arrow indicates the component of induction mapped.

S6. Micromagnetic simulations of hybrid domain walls

Micromagnetic simulations were performed using Mumax3 to compare to experimental observations. The details of the micromagnetic simulations are given in Appendix B but are also summarised here for the 5 \times , 10 \times and 15 \times repeat structures respectively as: $M_s = 1 \text{ MA m}^{-1}$, 1 MA m^{-1} and 1.2 MA m^{-1} ; $K_u = 0.829 \text{ MJ m}^{-3}$, 0.711 MJ m^{-3} and 0.622 MJ m^{-3} ; $D = 0.825 \text{ mJ m}^{-2}$, 0.707 mJ m^{-2} and 0.619 mJ m^{-2} ; and $A = 10 \text{ pJ m}^{-1}$ for all three. Fig. S6(a, c, e) show arrow plots indicating the direction of the magnetisation in each layer, in this projection M_x and M_z are given by the direction of the arrows and M_y is given by the red to blue colour scale. Both the 10 \times S6(c) and 15 \times S6(e) simulations show hybrid type walls with both Néel and Bloch sections forming a flux closure configuration. The 5 \times simulation is of pure Néel type with a

very slight twist away from pure Néel in the top most layer, where in Fig. S6(a) the arrow representing the left-hand side wall is slightly blue and the right-hand side wall is slightly red indicating non-zero M_y . This very slight surface twist occurs in simulations just below the threshold where the DMI induced field overcomes the dipolar interlayer field to stabilise pure homochiral Néel type walls. The right-hand side of Fig. S6(b, d, f) shows the normalised magnetisation of the wall averaged through the thickness. The peak of the M_y curve in each graph is equivalent to the ratio t_B/t quoted in the main paper. For the 5× sample S6(b) t_B/t is 0.04, 10× sample S6(d) t_B/t is 0.16 and 15× sample (d) t_B/t is 0.19. These values are summarised, along with the corresponding experimental measurements, in the table in Fig 6(c) of the main text.

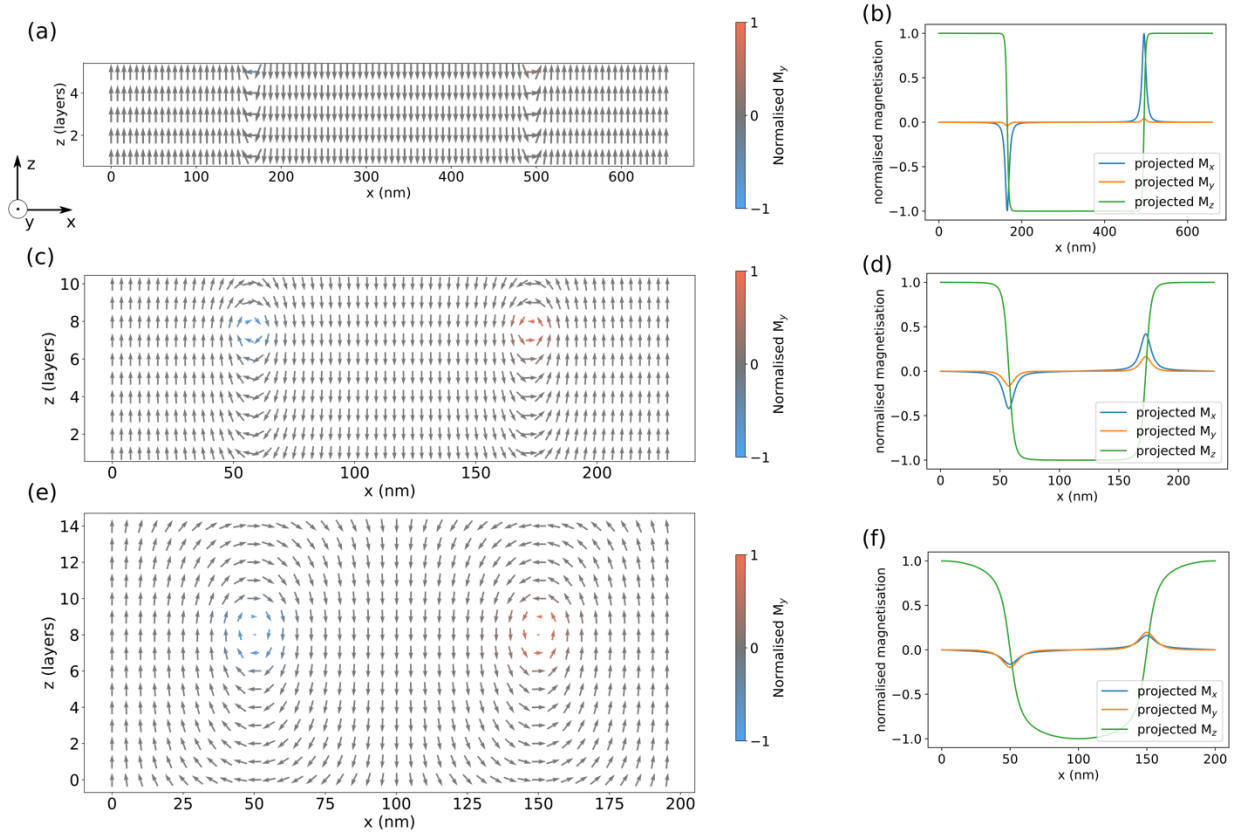


Figure S6. (a) arrow plot of the cross-section of simulated domain wall in the 5× sample and (b) graph of the thickness projected and normalised M_x , M_y and M_z components. (c) and (d) show the same quantities for the 10× sample and (e) and (f) for the 15× sample.

S7. Curves of A vs Δ generated from micromagnetic simulations

As discussed in the main text, the Lorentz microscopy technique of DPC has sufficient spatial resolution to measure the width of domain walls – even narrow walls only 10 nm and under, such as the ones present in these skyrmionic multilayer materials. The width parameter we measure, Δ , is related to the wall width, w . In the classical uniform film case, $w = \sqrt{A/K}$ where K is the anisotropy of the wall magnetization. Determination of Δ is hence interesting as it provides access to A . However, due to the more complex structure and energy balance of these domain walls in multilayers, it is challenging to identify the anisotropy appropriate for the wall itself. Therefore, to estimate A we have performed a set of micromagnetic simulations

with all parameters as detailed in Appendix B, except A which was varied between 3 and 20 pJm^{-1} . For every value of A , the system was allowed to relax and then from each relaxed state Δ was measured to produce the curves of A versus Δ shown in Fig. S7 – which follow the expected square root trend. These graphs suggest that the A in these magnetic multilayer systems is around 12 pJm^{-1} , in the expected range for such films. Additionally, micromagnetics also predicts that this slight increase in A would not change the t_B/t ratio of simulations of either the 10 \times or 15 \times sample – in fact over the A range simulated, the t_B/t ratio only differs significantly for the lowest value of $A = 3 \text{ pJm}^{-1}$.

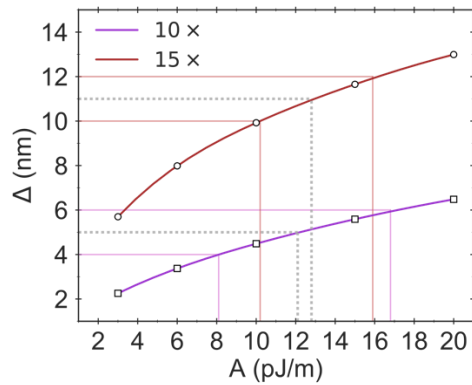


Figure S7. Graph of domain wall width parameter Δ versus A generated from micromagnetic simulations for the 10 \times and 15 \times repeat layer structures – dashed grey line indicates experimental wall width matched to the predicted A for this width.